3D+time acquisitions of 3D cell culture by means of lens-free tomographic microscopy

Anthony Berdeu, Bastien Laperrousaz, Thomas Bordy, Sophie Morales, Xavier Gidrol, Nathalie d'Hahan, Cédric Allier

3D+time acquisitions of 3D cell culture by means of lens-free tomographic microscopy

Anthony Berdeu[1], Bastien Laperrousaz[2], Thomas Bordy[1], S. Morales[1], Xavier Gidrol[2], Nathalie Picollet-D'hahan[2], and Cédric Allier[1]

[1] *Univ. Grenoble Alpes, CEA, LETI, DTBS, LISA, F-38000 Grenoble, France.*
[2] *Université Grenoble-Alpes, CEA, BIG, INSERM, F-38054 Grenoble, France*

1. ABSTRACT

We propose a three-dimensional (3D) imaging platform based on lens-free microscopy to perform multi-angle acquisitions on 3D cell cultures embedded in extracellular matrix (ECM). We developed algorithms based on the Fourier diffraction theorem to perform fully 3D reconstructions of biological samples and we adapted the lens-free microscope to incubator conditions. Here we demonstrate for the first time, 3D+time lens-free acquisitions of 3D cell culture over 8 days directly into the incubator. The 3D reconstructed volume is as large as ~5 mm^3 and provides a unique way to observe in the same 3D cell culture experiment multiple cell migration strategies. Namely, in a 3D cell culture of prostate epithelial cells embedded within a Matrigel® matrix, we are able to distinguish single cell 'leaders', migration of cell clusters, migration of large aggregates of cells, and also close-gap and large-scale branching. In addition, we observe long-scale 3D deformations of the ECM that modify the geometry of the 3D cell culture. Interestingly, we also observed the opposite, *i.e.* we found that large aggregates of cells may deform the ECM by generating traction forces over very long distances. In sum we put forward a novel 3D lens-free microscopy tomographic technique to study the single and collective cell migrations, the cell-to-cell interactions and the cell-to-matrix interactions.

2. INTRODUCTION

Cell movement is a key feature of many physiological and pathological processes including development, morphogenesis, tissue repair and cancer invasion [1][2]. Complex multicellular dynamics and tissue remodeling are supported by both single cell and collective cell migration processes [3][4]. With the aim of observing these processes over very long periods of time (several days) and over very large fields of volume (several mm^3),

without any labelling, we present a 3D+time lens-free microscope. This development follows previous works on lens-free tomography [5][6] but our approach is different by several aspects. First, in order to obtain a better angular coverage of the scene, *i.e.* the Petri dish containing the 3D culture, we chose an azimuthal tomographic acquisition geometry. Next, we implemented several 3D holographic reconstruction algorithms based on the Fourier diffraction theorem [7] to obtain fully 3D reconstructions. Finally and importantly, we were able to diminish and control the temperature of the CMOS sensor facing the 3D cell culture by means of a laminar air flow. It enabled us to run the image sensor in continuous mode without heating up the cell culture, allowing performing for the first time, 3D+time lens-free acquisitions of 3D cell culture over several days directly into the incubator. In order to validate this novel mean of microscopy, we choose to study RWPE1 cells, a model for normal prostate epithelial cell behavior characterized by a polarized acinar morphology in 3D cultures [8][9]. RWPE1 cells have also been used as dynamic model of the signaling and interactions between organoids and mesenchyme that are required during organ development [10]. In this paper we present two experiments of 3D cell culture of RWPE1 cells, observed by mean of our 3D+time lens-free microscope over eight consecutive days. Being able to acquire volume as large as 4.86 mm^3 without any labelling over a period of time covering several days allowed us to observe a broad range of phenomena only present in 3D environment. For instance we observed migration of cell leaders, collective cell migration and close-gap branching. These observations support well established migration strategies [1][2]. In sum we demonstrate that the dynamic vision of cell culture in 3D environment can be nicely captured with this novel technique of 3D+time lens-free microscopy.

3. MATERIAL AND METHODS

3D Cell culture

A Matrigel® drop is deposited at the center of a Greiner petri dish (Sigma-Aldrich) and allows polymerizing for 30 minutes at 37°C. RWPE1 cells are then added at the surface of Matrigel® and allow to attach for 1 hour at 37°C. KSFM (Life Technologies) supplemented with 50 ng/mL Epidermal Growth Factor (Life Technologies), 2% Fetal Bovine Serum (Life Technologies) and 1% Penicillin-Streptomycin (Life Technologies) is subsequently added.

Experimental setup

The reconstruction of 3D objects requires multiplying the viewing angles. In our experimental bench (see Fig.1a), a stepper motor (ref. RS-PRO-535-0401) rotates the CMOS sensor (IDS UI-1492-LE – 29.4 mm^2, 3840×2748 monochromatic pixels, pixel pitch 1.67 µm - ref. UI-1942LE-M) and the multi-wavelength illumination source (LED Cree, ref. XLamp MC-E RGBW MCE4CT-A2, $\lambda_B = 450$ nm; $\lambda_G = 520$ nm; $\lambda_R = 640$ nm) around an axis orthogonal to the sensor plane, whereas the object remains static. The illumination is

tilted by an angle θ which, can be tuned in the range of 30 to 55°. To maximize the common portion of field of view in the consecutive acquisitions, the sensor is slightly shifted from the axis so that the projected hologram of the 3D object remains centered in the sensor field regardless of the angle φ around the 3D sample. Such a configuration is well adapted to standard containers such as Petri dishes. In order to acquire data on large periods of time without killing the cells, a thermal insulation from the CMOS sensor is performed with an air knife flowing in between the sensor and the Petri dish from a vein carved in the sample holder.

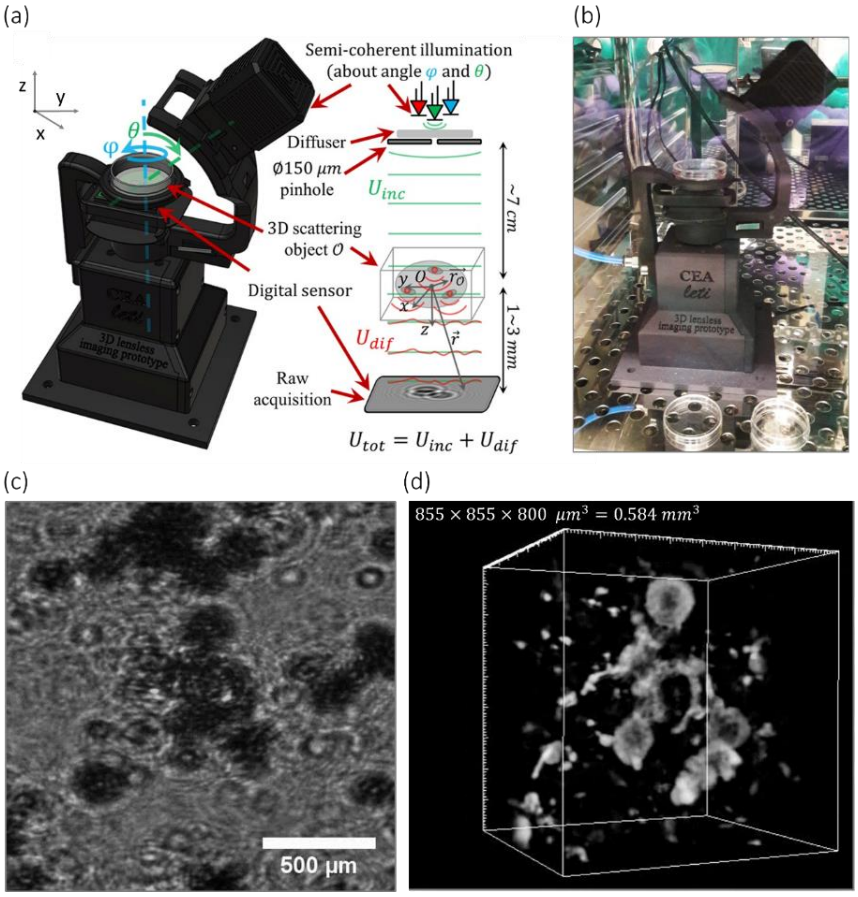

Figure 1. (a) Experimental setup dedicated to lens-free diffractive tomography and optical scheme of the system. The semi-coherent incident plane wave $U_{inc}$is scattered by the 3D sample which creates a diffracted waveU_{dif}. The sensor records the intensity of their interference: $I_d = |U_{tot}|^2$ with $U_{tot} = U_{inc} + U_{dif}$. (b) Picture of the experimental setup installed into the cell culture incubator. The Petri dishes are 35 mm in diameter. (c) Lens-free raw data acquisition of a 3D cell culture of RWPE1 cells (cropped image from a dataset of 3×31 acquisitions in RGB with 31 angles in $\varphi \in \{0°, 282°\}$ with $\Delta\varphi = 9.4°$). (d) Detail of the 3D reconstructed volume (0.584 mm^3) corresponding to the acquisition shown in (a).

Holographic 3D reconstruction

From an optical point of view, the microscope geometry does not have a reference arm as in standard off-line holography. This implies that the phase information of the total wave U_{tot} is lost as the sensor only records its intensity $I_d = |U_{tot}|^2$. U_{tot} is the interference of the incident wave U_{inc} produced by the LED and the diffracted wave U_{dif} scattered by the sample (see Fig. 1c and Fig. S2a): $U_{tot} = U_{inc} + U_{dif}$. A given dataset is consequently composed of a set of N intensities $I_d^j,\ j \in \|1, N\|$ recorded at different illumination positions (θ_j, φ_j) and at different wavelengths λ_j.

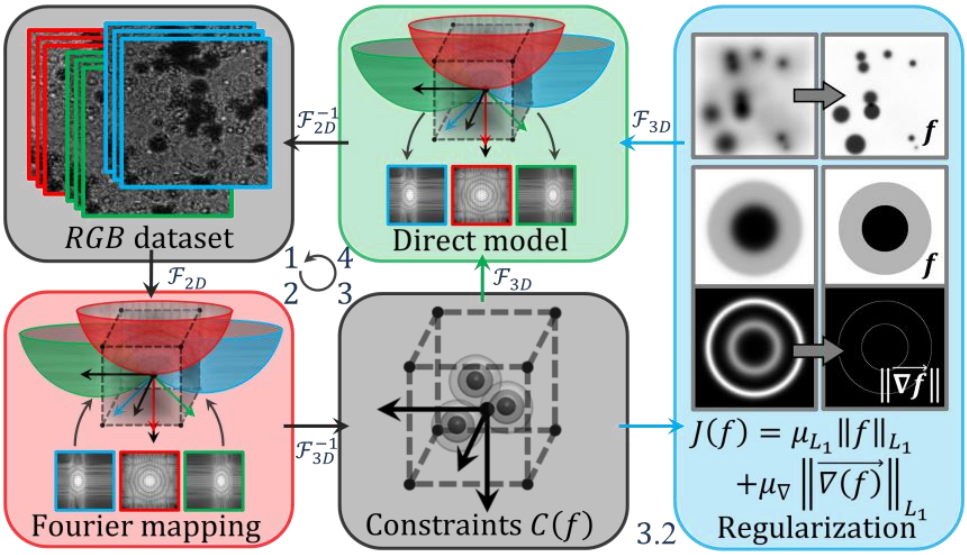

Figure 2. Scheme of the 3D reconstruction algorithms based on the regularized Gerchberg-Saxton algorithm. Step 1: The algorithm is initialized with a set of complex waves. Their modulus is directly the square root of the recorded intensities. Their unknown phase is initialized to 0. Step 2: These waves are used to map the 3D Fourier domain of the object $\hat{f}$ using the Fourier diffraction theorem. Step 3: Domain constraints are applied on the simulated object. Step 4: The new object is used to simulate a new set of complex waves using the Fourier diffraction theorem as a direct model. Step 1: The algorithm loops to start a new iteration. Data fidelity is performed by keeping the simulated phase and replacing the simulated modulus by the recorded dataset. In between the steps 3 and 4, an additional step can be added: Step 3.2. After applying the constraints, the object is regularized with a sparsity constraint on the object and its gradient.

The 3D diffracting sample must be reconstructed from this dataset. It is described by its scattering potential f defined at each point of space $\vec{r} = (x, y, z)$ by:

$$f(\vec{r}) = \left(\frac{n(\vec{r})}{n_0}\right)^2 - 1 \qquad (1)$$

where $n(\vec{r})$ is the local complex refractive index and n_0 is the refractive index of the surrounding medium.

In the hypothesis of transparent objects, we assume that the scattering potential is the same regardless of the illumination wavelength. For a monochromatic incident plane wave $U_{inc} = e^{i\overrightarrow{k_0}.\vec{r}}$ of wave vector $\overrightarrow{k_0} = \frac{2\pi n_0}{\lambda}(p_0, q_0, m_0)$ and under the first-order Born approximation, the Fourier diffraction theorem [11][12] links the 3D Fourier transform of the scattering potential *f* with the 2D Fourier transform of the diffracted field U_{dif} on a given plane at $z = z^+$(see Fig. S2):

$$\hat{f}(\alpha, \beta, \gamma) = \frac{4\pi}{ik_0^2} w(u, v) e^{-2i\pi w(u,v) z^+} \widehat{U}_{dif}(u, v; z^+) \qquad (2)$$

where (u, v, w) and (α, β, γ) are respectively the coordinates in the 2D Fourier space on the plane $z = z^+$ and in the 3D Fourier space of the object. They satisfy the following relationships:

$$\begin{cases} \alpha = u - u_0 \\ \beta = v - v_0 \\ \gamma = w - w_0 \end{cases} \text{ and } w(u, v) = \sqrt{\frac{n_0^2}{\lambda^2} - u^2 - w^2} \text{ with } (u_0, v_0, w_0) = \frac{n_0}{\lambda}(p_0, q_0, m_0) \qquad (3)$$

The Fourier transform and its inverse transform are here defined for a given function g as:

$$\mathcal{F}(g)(u) = \hat{g}(u) = \int_{-\infty}^{\infty} g(x) e^{-2i\pi ux}\, dx \text{ and } \mathcal{F}^{-1}(\hat{g})(x) = \int_{-\infty}^{\infty} \hat{g}(u) e^{2i\pi xu} du \qquad (4)$$

As shown schematically on Fig. 2, Eq. (3) implies that the two-dimensional surface $\widehat{U}_{dif}$ is mapped on a spherical cap (the so-called Ewald's sphere) into the 3D Fourier transform $\hat{f}$. This cap depends on $\overrightarrow{k_0}$ which gives its orientation via the direction (p_0, q_0, m_0) and its radius via the wavelength λ. The Fourier diffraction theorem can be used both for simulation (Fig. 2a - clockwise) from a numerical f to the corresponding diffracted wave U_{dif} and for direct reconstruction (Fig. 2b – counter-clockwise) from U_{dif} to f via a mapping of the Fourier coefficients of $\hat{f}$. Nevertheless, this last solution is ill-posed as it requires having access to both the amplitude and the phase of the different diffracted waves U_{dif}^j whereas only the intensity of the total wave $I_d = |U_{tot}|^2$ is recorded (Fig. 1). Here we have used a phase retrieval techniques to reconstruct the 3D experimental datasets (Figs. 1) based on a regularized Gerchberg-Saxton algorithm in which back and forth propagations between the experimental data and the 3D reconstructed object are performed to insure data fidelity with strong constraints and regularizations applied to the 3D diffracting objects. This algorithm is able to overcome the limitations raised by the lens-free microscope, *i.e.* the lack of phase information on the data and the limited angular coverage.

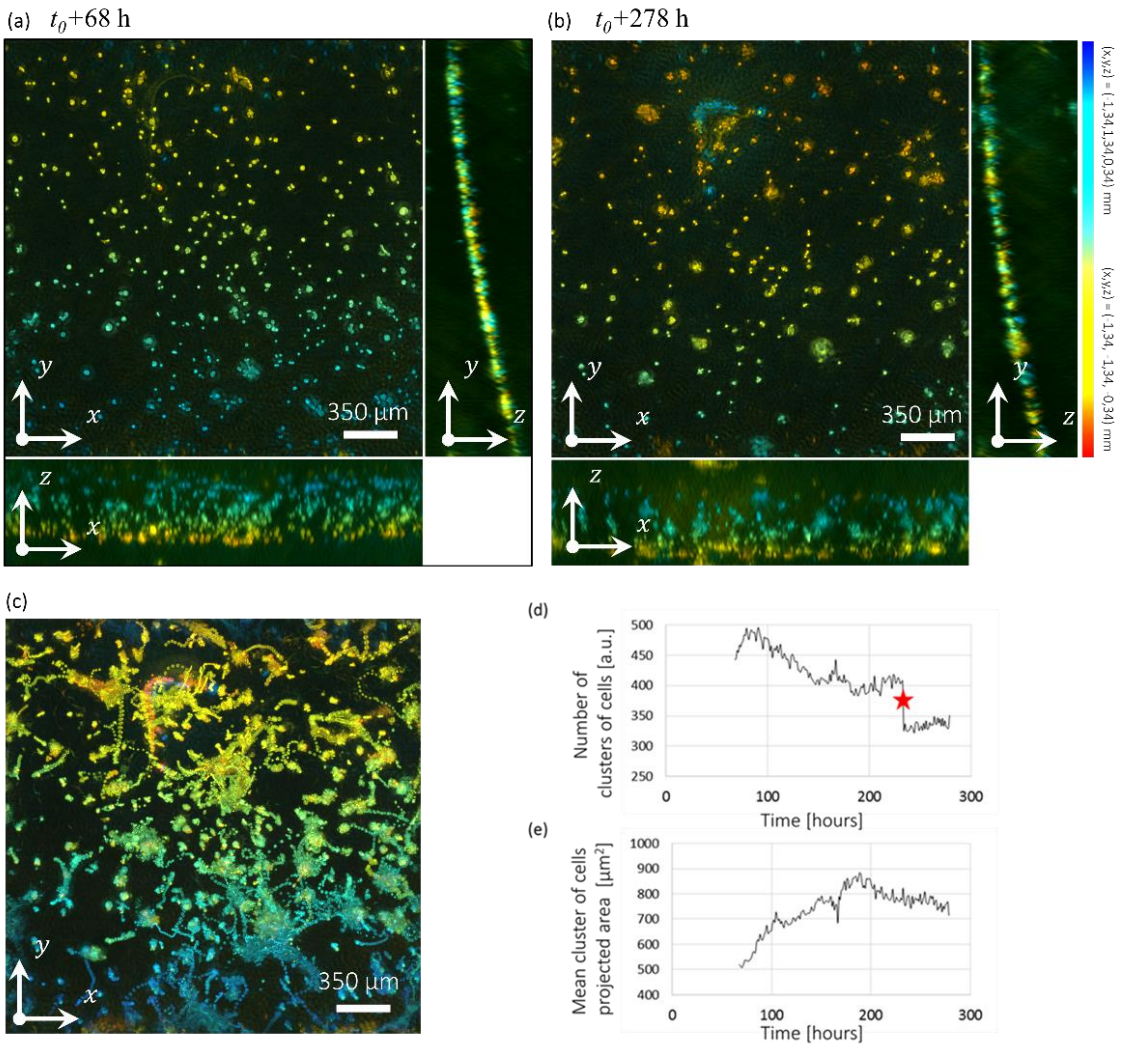

Figure 3. (a)(b) 3D orthogonal average intensity projection of the reconstructed volume of a 3D culture of RWPE1 cells. The two 3D reconstructions are taken from a 210 h long time-lapse acquisition at respectively t_0+68 h and t_0+278 h. The regularized Gerchberg-Saxton algorithm was run with the following parameters: $\varphi \in \{0°, 305°\}$, $\Delta\varphi = 9.8°, \theta = 45°$, 3D volume = $2.67 \times 2.67 \times 0.68 = 4.86$ mm^3, $800 \times 800 \times 128$ voxels of $3.34 \times 3.34 \times 5.32 = 60$ µm^3. The clusters of cells have been color-coded to visualize their position along the different axis of projection. The blue color encodes for the highest positions ($z = 0.34$ mm for the xy-view, $x = -1.34$ mm for the yz-view, $y = 1.34$ mm for the xz-view) and the red color encodes for the deepest positions ($z = -0.34$ mm for the xy-view, $x = 1.34$ mm for the yz-view, $y = -1.34$ mm for the xz-view). (c) Maximum intensity projection of the temporal stack for each pixel of the xy-view. The trajectory of isolated cells on large scales can be identified. (d) Number of detected objects as a function of the experiment time. The red star indicates the change of culture media at $t_0 = 234$ h when several clusters of cells have detached. (e) Mean projected area (xy-plane) of the detected cellular objects as a function of the experiment time.

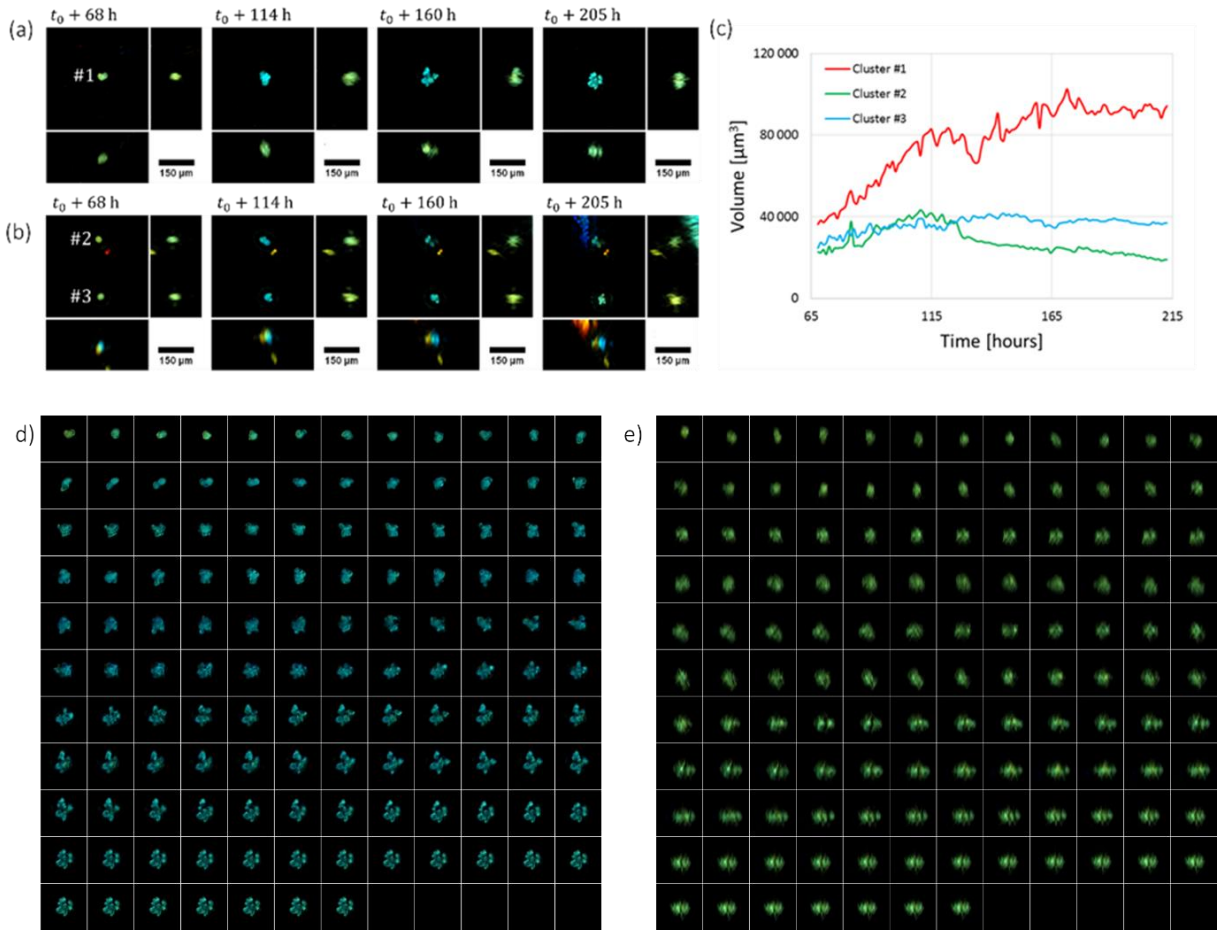

Figure 4 (a)(b) Time series of the reconstructed volume of three different clusters of cells with a time interval of $\Delta t = 46$ h. The color bar gives the depth in the volume for each view (see Fig. 3). (c) The volume of the three clusters of cells is plotted as a function of time. (d)(e) Time series of the cluster of cells shown in (a) in the xy-view and yz-view respectively ($\Delta t = 1$ h). Each cropped image is 170×170 μm^2.

4. RESULTS AND DISCUSSION

For the first time 3D time-lapse acquisition was obtained with our lens-free microscope on a 3D cell culture of RWPE-1 cells (Fig. 3). This time-lapse is composed of 3D reconstructions, based on a region of interest selected at the center of the sensor field of view. To reduce the computing time and the memory consumption, the final reconstructions are composed of 800×800×128 voxels of 3.34×3.34×5.32 µm^3 for a global volume of 2.67 × 2.67 × 0.68 = 4.86 mm^3. Thanks to the large reconstructed volume of ~5mm^3, it is hence possible to image simultaneously hundreds of cellular objects. This large field of view allows tracking cells on long distances, as emphasized on figure 3.c where the maximal values of the intensity projection during the temporal stack are kept. The cells displacements leave tracks on such a visualization. It can be seen that the

cells do not follow a random movement but are moving along extended organized trajectories. A first analysis consists in counting the number of cell clusters present in the 3D reconstructed volume as a function of time (figure 3.d) and measuring their size in terms of projected area (figure 3.e) in the xy-projection. At first, with the first cell divisions, the number of clusters reaches a maximum of 496 at $t_0 + 90$ h. But then, via cell divisions and successive merging, this number drops to 383 at $t_0 + 210$ h. In parallel, the average projected area of the clusters increases while the occupied area of the field of view reaches a plateau. This implies that the cells stop multiplying and favor global movements and merging.

Fig. 4 shows in detail the evolution in time of three different clusters of cells together with an estimation of their volume as a function of time. The reconstructions of this time-lapse are composed of 256 × 256 × 128 voxels of 1.67^3 μm^3 for a global volume of 427 × 427 × 214 = 3.9 10^7 μm^3. In this time-lapse, the three clusters that are blocked in the Matrigel® and grow inside the extracellular matrix (ECM). It is consequently possible to follow their development during the two weeks monitoring. The volumes are estimated according to a 3D segmentation performed using a simple thresholding algorithm. By monitoring their volume in figure 4.c, it appears that they grow before reaching a plateau and even retracting for the cluster 2. Cluster 1 volume grows linearly from 40 10^3 to 225 10^3 μm^3, reaching a plateau at $t_0 + 165$ h. In comparison, the initial growth of clusters 2 and 3 is negligible with a volume oscillating around 30 10^3 μm^3. When looking at the very large number of clusters present in the 3D reconstructed volume, the average size of the clusters has increased with time ($N > 300$, Fig. 3.d). Between two acquisitions separated by 211 hours shown in Figs. 3.ab respectively, the average projected area of the clusters has increased from 500 μm^2 to 710 μm^2 (see Fig. 3.e). A first population of isolated clusters has grown via cell proliferation just like the one depicted in Fig. 4.a. But interestingly other clusters have increased in size when merging.

5. CONCLUSION

In this paper we demonstrate that the novel 3D+time lens-free microscopy technique is a unique mean to provide new insights into spatial and temporal aspects of 3D cell culture. With respects to other 3D microscopy techniques, *e.g.* confocal microscopy, 3D digital in-line microscopy, and light-sheet microscopy, which provide much better resolution and specificity owing to fluorescence labelling, our 3D lens-free microscopy technique favors ease of use, label-free experimentation and allows the acquisition of very large 3D+time dataset. To our knowledge, our technique is the only one able at reconstructing very large volume of 3D cell culture (~5 mm^3) with by phase contrast imaging.

REFERENCES

[1] P. Friedl and D. Gilmour, “Collective cell migration in morphogenesis, regeneration and cancer.,” *Nat. Rev. Mol. Cell Biol.*, vol. 10, no. 7, pp. 445–57, Jul. 2009.

[2] O. Ilina and P. Friedl, “Mechanisms of collective cell migration at a glance.,” *J. Cell Sci.*, vol. 122, no. Pt 18, pp. 3203–8, Sep. 2009.

[3] S. Freitas-Rodríguez, A. R. Folgueras, and C. López-Otín, “The role of matrix metalloproteinases in aging: Tissue remodeling and beyond,” *Biochim. Biophys. Acta - Mol. Cell Res.*, vol. 1864, no. 11, pp. 2015–2025, 2017.

[4] E. Hannezo, C. L. G. J. Scheele, M. Moad, N. Drogo, R. Heer, R. V. Sampogna, J. van Rheenen, and B. D. Simons, “A Unifying Theory of Branching Morphogenesis,” *Cell*, vol. 171, no. 1, pp. 242–255.e27, 2017.

[5] S. O. Isikman, W. Bishara, S. Mavandadi, F. W. Yu, S. Feng, R. Lau, and A. Ozcan, “Lens-free optical tomographic microscope with a large imaging volume on a chip.,” *Proc. Natl. Acad. Sci. U. S. A.*, vol. 108, no. 18, pp. 7296–301, May 2011.

[6] C. Zuo, J. Sun, J. Zhang, Y. Hu, and Q. Chen, “Lensless phase microscopy and diffraction tomography with multi-angle and multi-wavelength illuminations using a LED matrix,” *Opt. Express*, vol. 23, no. 11, p. 14314, 2015.

[7] A. N. B. Berdeu, F. A. M. Omey, B. A. L. Aperrousaz, T. H. B. Ordy, X. A. G. Idrol, J. E. A. N. A. R. C. D. Inten, N. A. P. I. Hahan, and C. É. A. Llier, “Comparative study of fully three-dimensional reconstruction algorithms for lens-free microscopy,” vol. 56, no. 13, 2017.

[8] M. M. Webber, D. Bello, H. K. Kleinman, and M. P. Hoffman, “Acinar differentiation by non-malignant immortalized human prostatic epithelial cells and its loss by malignant cells,” *Carcinogenesis*, vol. 18, no. 6, pp. 1225–1231, 1997.

[9] D. Bello-DeOcampo, H. K. Kleinman, N. D. Deocampo, and M. M. Webber, “Laminin-1 and alpha6beta1 integrin regulate acinar morphogenesis of normal and malignant human prostate epithelial cells.,” *Prostate*, vol. 46, no. 2, pp. 142–53, 2001.

[10] L. E. O. Brien, M. M. P. Zegers, and K. E. Mostov, “Building epithelial architecture: insights from three-dimensional culture models,” vol. 3, no. July, pp. 1–7, 2002.

[11] E. Wolf, “Three-dimensional structure determination of semi-transparent objects from holographic data,” *Opt. Commun.*, vol. 1, no. 4, pp. 153–156, 1969.

[12] Y. Sung, W. Choi, C. Fang-Yen, K. Badizadegan, R. R. Dasari, and M. S. Feld, “Optical diffraction tomography for high resolution live cell imaging.,” *Opt. Express*, vol. 17, no. 1, pp. 266–277, 2009.

[13] P. Y. Liu, L. K. Chin, W. Ser, H. F. Chen, C.-M. Hsieh, C.-H. Lee, K.-B. Sung, T. C. Ayi, P. H. Yap, B. Liedberg, K. Wang, T. Bourouina, and Y. Leprince-Wang, “Cell refractive index for cell biology and disease diagnosis: past, present and future.,” *Lab Chip*, vol. 16, pp. 634–644, 2016.